

Superlubric Polycrystalline Graphene Interfaces

Xiang Gao

Tel Aviv University

Wengen Ouyang

Tel Aviv University <https://orcid.org/0000-0001-8700-1978>

Michael Urbakh (✉ urbakh@tauex.tau.ac.il)

Tel Aviv University <https://orcid.org/0000-0002-3959-5414>

Oded Hod

Tel Aviv University <https://orcid.org/0000-0003-3790-8613>

Article

Keywords: graphene interfaces, frictional properties, corrugated grain boundaries

Posted Date: March 24th, 2021

DOI: <https://doi.org/10.21203/rs.3.rs-345932/v1>

License:  This work is licensed under a Creative Commons Attribution 4.0 International License.

[Read Full License](#)

Version of Record: A version of this preprint was published at Nature Communications on September 28th, 2021. See the published version at <https://doi.org/10.1038/s41467-021-25750-w>.

Superlubric Polycrystalline Graphene Interfaces

Xiang Gao¹, Wengen Ouyang², Michael Urbakh^{1*}, Oded Hod¹

¹ Department of Physical Chemistry, School of Chemistry, The Raymond and Beverly Sackler Faculty of Exact Sciences and The Sackler Center for Computational Molecular and Materials Science, Tel Aviv University, Tel Aviv 6997801, Israel.

² Department of Engineering Mechanics, School of Civil Engineering, Wuhan University, Wuhan, Hubei 430072, China.

Abstract

The effect of corrugated grain boundaries on the frictional properties of extended graphitic contacts incorporating a polycrystalline surface are investigated. The friction is found to be dominated by shear induced buckling and unbuckling of corrugated grain boundary dislocations, leading to a nonmonotonic behavior of friction with normal load and temperature. The underlying mechanism involves two competing effects, where an increase of dislocation buckling probability is accompanied by a decrease of the dissipated energy per buckling event. These effects are well captured by a phenomenological two-state model, that allows for characterizing the tribological properties of any large-scale polycrystalline layered interface, while circumventing the need for demanding atomistic simulations. The resulting negative differential friction coefficients obtained in the high-load regime can reduce the expected linear scaling of grain-boundary friction with surface area and restore structural superlubricity at increasing length-scales.

*Corresponding author: Michael Urbakh

Email: urbakh@tauex.tau.ac.il

27 **Introduction**

28 Reduction of energy dissipation and wear is of critical importance and growing demand in a wide
29 range of areas, including mechanical, electronic, and biological systems. Compared to traditional
30 lubrication schemes, structural superlubricity, featured as extremely low friction due to the effective
31 cancellation of lateral forces at incommensurate crystalline contact interfaces, has emerged as a
32 novel route toward efficient reduction of friction and wear^{1,2}. Recent studies have reported
33 structural superlubricity in nano- and micro-sized monocrystalline samples of layered materials,
34 where misoriented lattices³⁻⁷ or mismatched lattice constants⁸⁻¹³ facilitate the necessary
35 incommensurability. However, scaling up structural superlubricity towards macroscopic
36 dimensions inevitably involves forming junctions between surfaces of polycrystalline nature.

37 The simplest example of polycrystalline monoatomic two-dimensional (2D) surface is
38 polycrystalline graphene (PolyGr), which is composed of randomly shaped and oriented single
39 crystalline graphene patches separated by sharp grain boundaries (GBs). The latter, are
40 characterized by chains of lattice dislocations often including pentagon-heptagon pairs¹⁴. Since the
41 friction between misaligned graphitic patches is known to be negligibly small³, one could expect
42 that superlubricity would prevail also in large-scale PolyGr interfaces, pending that the patch
43 dimensions remain in the nanoscale. However, PolyGr GBs often exhibit out-of-plane
44 corrugation¹⁵⁻¹⁷, that may introduce substantial friction¹⁸⁻²⁰ and enhance wear²¹. To control and
45 eliminate such undesired effects one must fully understand the mechanisms underlying energy
46 dissipation at elongated graphene GBs. This, in turn, requires elucidating collective effects between
47 different topological defects along the GBs under persistent shear.

48 Here, we reveal that collective dynamic effects at PolyGr GBs lead to unusual nonmonotonic
49 variation of the friction with normal load and temperature. Notably, at room temperature or above
50 we find a monotonic decrease of friction with the external normal load for the systems considered,
51 resulting in negative differential friction coefficients. The discovered phenomenon is of general
52 nature and is expected to occur in other polycrystalline layered materials that demonstrate out-of-
53 plane GB deformations. Moreover, the knowledge gained in this study may provide insights
54 regarding universal mechanisms of energy dissipation appearing in extended multi-contact rough
55 interfaces, where the formation and rupture of contacts dictates the static and kinetic friction²²⁻²⁷.

56 Results

57 Our model system for studying the friction over extended graphene GBs is shown in Fig. 1a. From
58 top to bottom, the system consists of a slider composed of three Bernal stacked pristine graphene
59 (PrisGr) layers orientated at $\theta_0 = 38.2^\circ$, a layer of PolyGr including two patches with orientation
60 angles of $\theta_1 = 0^\circ$ (left and right parts of the supercell, see Fig. 1b) and $\theta_2 = 8^\circ$ (middle section of
61 the supercell, see Fig. 1b), and a substrate consisting of two Bernal stacked PrisGr layers with
62 orientation angle $\theta_3 = 0^\circ$. All orientation angles are measured between the sliding direction (x axis)
63 and the armchair direction of the lattice of the relevant layer. The PolyGr layer contains two GBs
64 composed of lines of separated pentagon-heptagon pair dislocations along the GB (y axis) direction
65 (Fig. 1b). The dislocations introduce in-plane strain to the otherwise hexagonal lattice, which is
66 partially relieved via out-of-plane deformations¹⁸. The average corrugation of the free surface
67 (bottom three layers without the slider) reaches $\sim 1.4 \text{ \AA}$, consistent with previous experimental
68 measurements¹⁶. After annealing the entire six layers structure at 1000 K and zero normal load,
69 most of the dislocations exhibit considerable out-of-plane deformations, protruding upward or
70 downward as shown in the lower panel of Fig. 1b. Imposing normal load, by adding a uniform force
71 in the vertical direction to each atom in the top layer, reduces the average corrugation of the
72 dislocations from 0.5 \AA to 0.1 \AA as normal load increases from 0 to 1.9 GPa (Fig. 1b).

73 In the sliding simulations, normal loads up to ~ 2.3 GPa are applied. The top layer is kept rigid and
74 is shifted with a constant velocity of $v_0 = 5 \text{ m/s}$ in the x direction (Fig. 1d). Since the slider layers
75 are incommensurate with both PolyGr patches, the shear plane appears at the interface of the third
76 layer of the slider and the PolyGr layer. The generated heat is removed from both slider and
77 substrate without affecting the dynamics at the shear interface. See Methods and Supplementary
78 Note 1 for further details regarding the simulation model and protocols.

79 The dependence of the interfacial friction between the PrisGr and PolyGr surfaces on the normal
80 load and temperature are presented in Fig. 2a, b, respectively. Fig. 2a presents the load dependence
81 of the friction for several temperatures in the range 0 – 300 K. At zero temperature the friction
82 shows nonmonotonic behavior with load, where an expected friction increase with load is observed
83 up to ~ 0.5 GPa followed by friction reduction at higher loads. When the temperature is increased
84 to 50 K the overall friction increases and the maximal friction point shifts towards lower normal
85 loads. When the temperature is further increased to 150 K the maximum completely disappears and
86 the friction reduces monotonically with the normal load exhibiting negative differential friction
87 coefficients across the entire load range considered^{13,28}. At 300 K a similar behavior is observed

88 with overall reduced friction. The differential friction coefficients calculated in this case are
89 between -1.16×10^{-4} and -8.5×10^{-6} .

90 The friction-temperature relation, shown in Fig. 2b, exhibits similar behavior. At zero normal load,
91 the friction presents a nonmonotonic curve with a maximum value at $T = 150$ K. As the normal load
92 increases, the overall friction force decreases and the position of maximal friction shifts to lower
93 temperatures.

94 The nonmonotonic behavior in the friction-load and friction-temperature relations suggests that
95 there are two competing effects that dictate the overall energy dissipation throughout the sliding
96 process. To understand the underlying mechanisms, we examine the simple case of friction-load
97 relation in the absence of thermal effects, i.e. at $T = 0$ K. Analyzing the energy dissipation routes
98 by calculating the steady-state dissipation power through the damped layers in different directions
99 (Fig. 3a) demonstrates that energy dissipation is dominated by out-of-plane atomic motion at the
100 GBs regions (see Fig. 3a, b and Supplementary Note 3). Based on this understanding we tracked
101 the vertical motion of the atoms with maximal root-mean-square (RMS) corrugation (calculated as
102 the time-averaged RMS displacement) in each dislocation during sliding (Fig. 3c). The RMS
103 corrugation is calculated by temporal averaging the out-of-plane displacements of each atom within
104 a given dislocation over the entire trajectory. Interestingly, we observe that at zero and 0.6 GPa
105 normal load several dislocations undergo dynamic snap-through buckling between an upward
106 protrusion state and a downward protrusion state (top and middle panels in Fig. 3c and
107 Supplementary Movies 1 and 2), which resembles the dynamics of an arched beam. These dynamic
108 buckling dislocations correspond to the high energy dissipation sites shown in Fig. 3b and
109 Supplementary Fig. 6. Notably, for dislocations that do not buckle during sliding, the associated
110 energy dissipation is very low, comparable to that in the grain areas. This demonstrates that the
111 surface corrugation of the GB alone does not produce significant dissipation and the snap-through
112 buckling of dislocations provides the major contribution to the enhanced friction exhibited by GBs
113 and to the corresponding nonmonotonic frictional dissipation behavior with normal load.

114 The dynamic snap-through buckling phenomenon indicates that the GB dislocations exhibit bi-
115 stable behavior characterized by the upward and downward protruding states separated by transition
116 energy barriers. An estimate of the corresponding barrier heights can be obtained by considering
117 the thermally activated dislocation buckling process in the absence of sliding. To this end, we
118 performed room temperature ($T = 300$ K) equilibrium molecular dynamic simulations of the six-
119 layered model system presented in Fig. 1, without applying any shear force. During the dynamics,
120 we followed the z coordinate of the atom with largest RMS corrugation in the dislocation region. A

121 typical example of such an atomic trajectory is presented in the inset of Fig. 4a showing clear
122 evidence of a mechanical bistability. The buckling Helmholtz free-energy²⁹, $A(\Delta z)$, profile can be
123 extracted from such trajectories by evaluating the probability density distribution, $\rho(\Delta z)$, of finding
124 this atom at a displacement of Δz away from the average height of the two PolyGr layer grains, and
125 substituting it in the relation $A(\Delta z) = -k_B T \ln[\rho(\Delta z)]$, where k_B is the Boltzmann constant. From
126 this profile the snap-through buckling process barrier heights can be readily extracted (see e.g. ΔE_b
127 and ΔE_u in Fig. 4a). We note that the transition energy barriers obtained from this method compare
128 well with those obtained using nudged elastic band (NEB) calculations (see Supplementary Note
129 5). The corresponding distribution of dislocation barriers appears in Fig. 4b. Notably, by performing
130 the same analysis under an external normal load we find that, along with the reduction of the spatial
131 corrugation of the dislocations (Fig. 1c), the average transition energy barrier between the upward
132 and downward protruding states and the number of dislocations with substantial barrier reduce as
133 well (Fig. 4c). Furthermore, we find a positive correlation between the transition energy barrier for
134 (un)buckling of a given GB dislocation and its out-of-plane corrugation (Fig. 4d).

135 This analysis allows us to identify the competing effects leading to the nonmonotonic friction
136 dependence on normal load appearing in Fig. 2a. At zero temperature ($T = 0$ K) the snap-through
137 bi-stability can be triggered by the sliding process via two main effects: (i) variation of the snap-
138 through barrier along the scan-line; and (ii) shear-force induced out-of-plane motion of atoms in
139 the dislocation region. At zero normal load, only a few shear-induced buckling events occur (see
140 top panel in Fig. 3c and Supplementary Movie 1) due to the relatively high energy barriers with
141 respect to the kinetic energy of the dislocation atoms. However, once triggered, each snap-through
142 event generates a large kinetic energy pulse (see top panel in Fig. 3d) that dissipates through inter-
143 and intralayer interactions. Increasing the normal load to 0.6 GPa results in a reduction of the
144 transition energy barriers and hence an increase in the fraction of buckling dislocations (see middle
145 panel in Fig. 3c and Supplementary Movie 2). This, in turn, leads to more frequent kinetic energy
146 pulses (see middle panel in Fig. 3d), consistent with the observed enhancement in the out-of-plane
147 energy dissipation and friction (upward facing blue triangles in Fig. 3a). When the normal load is
148 further increased to 1.9 GPa, the barrier height becomes comparable to the kinetic energy of the
149 dislocation atoms and the transition between upward and downward protruding states occurs
150 smoothly (showing no abrupt kinetic energy pulses, see bottom panel in Fig. 3d) with lower
151 amplitude and little energy dissipation (see bottom panel in Fig. 3c and Supplementary Movie 3).
152 This results in reduced out-of-plane dissipation and friction as seen in Fig. 3a at this load. A similar
153 behavior is obtained at a higher temperature of $T = 50$ K, however with a downshift of the friction

154 maximum due to thermal activation of the buckling process (see Fig. 2a and Supplementary Movie
155 4). At even higher temperatures of $T = 150$ K and 300 K, most of the dislocations buckle already
156 at zero normal load and the friction force decreases monotonically with increasing load due to the
157 reduction of the transition energy barriers (see Fig. 2a and Supplementary Movies 5 and 6).

158 Next, consider the nonmonotonic friction dependence on temperature (Fig. 2b). At low
159 temperatures ($T < 150$ K) and in the absence of normal load, thermal fluctuation can assist
160 overcoming the transition energy barriers for buckling during sliding, activating more dislocations
161 to buckle and increasing their snap-through frequency (see Supplementary Note 4 and
162 Supplementary Movie 4). Since each such event is accompanied by a sharp kinetic energy
163 dissipation pulse, the overall friction increases. As the temperature further increases, the thermal
164 energy, $k_B T$, becomes comparable to the energy barrier heights, leading to frequent spontaneous
165 buckling of dislocations between the two states (see Supplementary Note 4 and Supplementary
166 Movie 6). Correspondingly, less energy is invested by the sheared slider to induce dislocation
167 buckling, and the friction reduces. Therefore, we conclude that the nonmonotonic friction-
168 temperature relation stems from two competing effects, i.e. thermally assisted shear-induced
169 buckling vs. thermally dominated spontaneous buckling. A similar behavior is obtained at higher
170 normal loads, however the corresponding reduced barriers result in lower overall friction and a
171 downshift of the friction maximum (Fig. 2b).

172 To evaluate the general nature of this frictional behavior we considered also a PolyGr surface of a
173 smaller GB misfit angle of $\theta_2 = 2.5^\circ$ that exhibits higher GB corrugation than the $\theta_2 = 8^\circ$ case. We
174 find that the overall qualitative dependence of the friction on the normal load and temperature is
175 preserved with some quantitative modifications due to the increased barrier heights (see Fig. 2a and
176 Supplementary Note 6).

177 We note that the similar nonmonotonic behaviors of the friction with normal load and with
178 temperature, presented in Fig. 2a, b, are not coincidental. In the load-dependence case, the thermal
179 energy remains constant and the barrier heights are varied relative to it upon changing the external
180 load, whereas, in the temperature-dependence case the thermal energy is varied with respect to the
181 barrier heights by controlling the target temperature of the thermostats. The overall net effect is
182 very similar.

183 The dominance of the bi-stability mechanism on the frictional properties of the GBs allows us to
184 provide a simple and intuitive description of the tribological properties of this involved system.
185 This is achieved by mapping the complex out-of-plane buckling dynamics onto a simple two-state
186 model, associated with the upward and downward protruding states of a single dislocation, which

187 are separated by a transition energy barrier (TEB, see Fig. 4a), $\Delta E^n(\sigma)$, n being the dislocation
 188 number. Based on our simulation results, we introduce the following assumptions: (i) the
 189 distribution of TEBs corresponding to different dislocations is uniform within a given range (Fig.
 190 4b); (ii) the reduction of the TEB of any given dislocation with the normal load is approximately
 191 linear (Fig. 4c); and (iii) the TEB of all dislocations depend on the relative position, x , of the
 192 interfacial layers at the sliding contact, such that $\Delta E^n(\sigma) \rightarrow \Delta E^n(x, \sigma)$. The latter assumption
 193 results from the variation of the Pauli repulsions experienced by the two interfacial layers as their
 194 hexagonal lattices slide across each other. Note that $\Delta E_{\max}^n(\sigma) \geq \Delta E^n(x, \sigma) \geq \Delta E_{\min}^n(\sigma)$, where
 195 $\Delta E_{\max}^n(\sigma)$ and $\Delta E_{\min}^n(\sigma)$ are the maximal and minimal buckling TEB heights encountered along
 196 one period of the sliding path, set by the hexagonal lattice periodicity of the pristine lower surface
 197 of the slider.

198 Considering first the zero-temperature case, for a given normal load, σ , buckling will occur only in
 199 dislocations for which the TEB vanishes along the sliding path, $\Delta E_{\min}^n(\sigma) = 0$. The energy
 200 dissipated once buckling occurs equals the energy invested to induce the buckling, which in turn,
 201 is given by the maximal TEB height along the sliding path, $\Delta E_{\max}^n(\sigma)$. As stated above, the TEBs
 202 are assumed to reduce linearly with the normal load such that:

$$203 \quad \begin{cases} \Delta E_{\min}^n(\sigma) = \Delta E_{\min}^n(0) - \alpha_1 \sigma \\ \Delta E_{\max}^n(\sigma) = \Delta E_{\max}^n(0) - \alpha_2 \sigma \end{cases} \quad (1)$$

204 The slopes, α_i , and $\Delta E^n(0)$ can be estimated from our simulation results (Fig. 4c). The average
 205 load dependent friction force can then be estimated as follows:

$$206 \quad F_f(\sigma) = \sum_n^N \frac{\Delta E_{\max}^n(\sigma)}{\Delta x} [1 - H(\Delta E_{\min}^n(\sigma))] H(\Delta E_{\max}^n(\sigma)). \quad (2)$$

207 Here, $\Delta E_{\max}^n(\sigma)/\Delta x$ is the average friction force induced by the buckling of the n^{th} dislocation,
 208 calculated as the dissipated energy per period, the first Heaviside step function $H(x)$ takes into
 209 account that at zero temperature only dislocations of vanishing TEB buckle, the second Heaviside
 210 function assures that unphysical negative TEB values are not considered, and the sum runs over all
 211 N dislocations. Eq. (2) demonstrates that the nonmonotonic friction dependence on external load
 212 originates from two competing effects: (i) the increase of number of active dislocations
 213 (dislocations with vanishing $\Delta E_{\min}^n(\sigma)$) with normal load; and (ii) decrease of the dissipated energy
 214 per buckling event ($\Delta E_{\max}^n(\sigma)$).

215 For simplicity, the sum appearing in Eq. (2) can be approximated via integration. To this end, we
 216 further assume that there is a linear relation between the maximal and minimal values of the TEB
 217 along a sliding period at zero normal load:

$$218 \quad \Delta E_{\min}^n(0) = \beta \Delta E_{\max}^n(0) - c_0 \quad (3)$$

219 Together with Eq. (1) this yields the following relation between the maximal and minimal values
 220 of the TEB along a sliding period at any finite normal load, σ :

$$221 \quad \Delta E_{\min}^n(\sigma) = \beta \Delta E_{\max}^n(0) - \alpha_1 \sigma - c_0 = \beta \Delta E_{\max}^n(\sigma) - c_0 - (\alpha_1 - \alpha_2 \beta) \sigma. \quad (4)$$

222 With this, we may approximate Eq. (2) as follows:

$$223 \quad F_f(\sigma) \approx N \int \frac{\Delta E_{\max}(\sigma)}{\Delta x} [1 - H(\Delta E_{\min}(\sigma))] H(\Delta E_{\max}(\sigma)) P_b(\Delta E_{\max}(0)) d\Delta E_{\max}(0), \quad (5)$$

224 where we introduced the probability density distribution of the TEB heights $P_b(\Delta E_{\max}(0))$
 225 (assumed to be normalized to 1) and used the fact that $d\Delta E_{\max}(0) = d\Delta E_{\max}(\sigma)$, per Eq. (1). Based
 226 on our simulation results (Fig. 4b), we may approximate the probability distribution $P_b(\Delta E_{\max}(0))$
 227 to vanish outside a finite range $[\Delta E_1, \Delta E_2]$ and be uniform within it. Using this in Eq. (5) and
 228 performing the integral results in the black line appearing in Fig. 2c, which correspond well, both
 229 qualitatively and quantitatively, with the simulation results.

230 At finite temperatures, buckling is not limited to zero barrier dislocations, and can occur also for
 231 finite barrier dislocations. To account for this, we introduce the survival probability function,
 232 $p(t, \sigma)$, that describes the probability of a given dislocation not to buckle up to time t , along one
 233 sliding period. Assuming that the dislocations are independent, this can be described as a first-order
 234 rate equation:

$$235 \quad \frac{d}{dt} p(t, \sigma) = -f_0 e^{\frac{-\Delta E^n(t, \sigma)}{k_B T}} p(t, \sigma), \quad (6)$$

236 where f_0 is constant, $\Delta E^n(t, \sigma)$ is the instantaneous energy barrier along one sliding period. For
 237 sliding at constant velocity, v , we may replace the time coordinate with the spatial coordinate using
 238 $t = x/v$, yielding:

$$239 \quad \frac{d}{dx} p(x, \sigma) = -\frac{f_0}{v} e^{\frac{-\Delta E^n(x, \sigma)}{k_B T}} p(x, \sigma). \quad (7)$$

240 Assuming a linear variation of $\Delta E^n(x, \sigma)$ between $\Delta E_{\max}^n(\sigma)$ and $\Delta E_{\min}^n(\sigma)$:

$$241 \quad \Delta E^n(x, \sigma) = \Delta E_{\max}^n(\sigma) - \frac{x}{\Delta x} [\Delta E_{\max}^n(\sigma) - \Delta E_{\min}^n(\sigma)], \quad (8)$$

242 Eq. (6) can be solved analytically, yielding (for an initial condition of $p(0, \sigma) = 1$):

$$p(x, \sigma) = e^{-c_1(\sigma) \left[e^{\frac{-\Delta E^n(x, \sigma)}{k_B T}} - e^{\frac{-\Delta E_{\max}^n(\sigma)}{k_B T}} \right]}, \quad (9)$$

where $c_1(\sigma) = f_0 k_B T \Delta x / [\Delta E_{\max}^n(\sigma) - \Delta E_{\min}^n(\sigma)] v$.

The probability density distribution of the dislocation to buckle at position x along the sliding path is given by the corresponding reduction of the survival probability at this point, namely $f(x, \sigma) = -dp(x, \sigma)/dx$. With this, the energy dissipated by an individual dislocation due to shear induced buckling over a full sliding period is given by:

$$\Delta w(\sigma) = \int_0^{\Delta x} dx [\Delta E_{\max}^n(\sigma) - \Delta E^n(x, \sigma)] f(x, \sigma) H(\Delta E^n(x, \sigma)), \quad (10)$$

where $\Delta E_{\max}^n(\sigma) - \Delta E^n(x, \sigma)$ is the dissipated elastic energy invested in depressing the dislocation if it buckles at point x and the Heaviside step function screens unphysical negative barrier heights. Note that this derivation follows the spirit of the Prandtl-Tomlinson model at finite temperatures³⁰⁻³². The resulting expression for $\Delta w(\sigma)$ (see Supplementary Note 7) replaces the term $\Delta E_{\max}^n(\sigma)$ in Eq. (5) for the zero-temperature case and the calculation for the friction force proceeds accordingly. The results of this calculation, appearing in Fig. 2c, d, show good correspondence with the simulation results, both for the normal load dependence at fixed temperature (Fig. 2c) and for the temperature dependence at fixed normal load (Fig. 2d). It should be noted that when fitting the model to the simulation results, the periodicity Δx was chosen to be 10.8 Å, approximately 1/3 of the period of the bottom PrisGr layer of the slider, reflecting the fact that dislocations may buckle more than once per sliding period (see Fig. 3c). Therefore, we conclude that the nonmonotonic frictional dependence on temperature originates from similar competing effects: (i) increase of buckling probability with temperature; and (ii) decrease in dissipated energy per buckling event when buckling occurs earlier along the path. The latter results from the fact that thermal fluctuations assist overcoming the barrier hence less energy needs to be invested (and lost) by the shear process in order to buckle.

Discussion

Notably, one of the important assumptions underlying the phenomenological model is the independence of buckling events occurring at different dislocation centers. The good agreement that the model achieves with elaborate simulation results of various corrugated GBs indicates the validity of this assumption for realistic polycrystalline surfaces. This suggests that the frictional dissipation of corrugated GBs should be proportional to their overall length that, in turn, grows linearly with the overall contact area, S_{tot} . To demonstrate this, we note that the perimeter of an

274 individual grain, i.e. the length of its GB, L_{grain} , is proportional to the square root of its surface
 275 area. Marking $P(S)$ as the probability density function of obtaining a grain of area S , the average
 276 grain area is given by $\bar{S}_{\text{grain}} = \int P(S)SdS$ and the corresponding average boundary length per grain
 277 is $\bar{L}_{\text{grain}} \propto \int P(S)\sqrt{S}dS$. The average number of grains is therefore given by $N_{\text{grain}} = S_{\text{tot}}/\bar{S}_{\text{grain}}$,
 278 yielding an average overall GB length of $L_{\text{tot}} \propto \zeta N_{\text{grain}} \bar{L}_{\text{grain}} = \zeta (\bar{L}_{\text{grain}}/\bar{S}_{\text{grain}}) S_{\text{tot}}$, which is
 279 proportional to S_{tot} for any reasonable distribution of grain areas. Here, ζ is a constant pre-factor
 280 of $O(1)$ accounting for overlapping boundaries of adjacent grains. Given this length scaling, the
 281 friction coefficient under a given normal pressure, σ , will be proportional to the GB length per unit
 282 area: $\mu \propto L_{\text{tot}}/S_{\text{tot}} \propto \zeta (\bar{L}_{\text{grain}}/\bar{S}_{\text{grain}})$. This stems from the fact that the friction coefficient is
 283 defined as the ratio between the friction and normal forces, $\mu = F_f/F_N$, where $F_f \propto L_{\text{tot}}$ and $F_N =$
 284 $S_{\text{tot}}\sigma$.

285 Aiming to scale-up structural superlubricity in layered material interfaces implies the inevitable
 286 appearance of GBs at the sliding interface. As shown above, the scaling of their dissipative
 287 contribution with contact area is stronger than the sublinear scaling found for pristine
 288 incommensurate layered contacts^{33,34}. Nevertheless, the predicted nonmonotonic frictional
 289 dependence on normal load and temperature leads to negative differential friction coefficients at
 290 the high normal load regime. This, in turn, opens the way to achieve large-scale superlubricity by
 291 reducing the excess friction associated with each GB. The underlying mechanism, which is valid
 292 for any corrugated polycrystalline layered interface, involves two competing effects: an increase of
 293 buckling probability accompanied by a decrease of the dissipated energy per buckling event with
 294 normal load and/or temperature. This mechanism is quite different from simple steric hindrance
 295 considerations induced by rigid corrugated obstacles³⁵. For incommensurate contacts, the
 296 contribution of flat GB geometries (where buckling events are absent) to the overall friction is
 297 small, as their tribological properties resemble those of a pristine interface. Therefore, the
 298 phenomenological model developed herein can serve as an efficient tool to characterize the
 299 frictional properties of complex interfaces consisting of involved GB geometries, as long as friction
 300 is dominated by buckling events. This may help reducing the dependence on explicit demanding
 301 simulations of large-scale polycrystalline mosaic interfaces and focus computational efforts on
 302 understanding specific microscopic mechanisms of interest.

303 304 **Methods**

305 The structure of the PolyGr layer is generated using a Voronoi tessellation method developed by
 306 Shekhawat^{36,37}, which introduces minor strain effect (see Supplementary Note 1 for details).

307 Periodic boundary conditions are applied for all six layers along both lateral directions. The
308 intralayer and interlayer interactions are modeled with the second-generation reactive empirical
309 bond order (REBO) potential³⁸ and the registry-dependent interlayer potential (ILP)³⁹⁻⁴³ with the
310 refined parameters⁴³ that is accurate also in the high pressure regime⁴⁴, respectively. All simulations
311 were performed using the LAMMPS package⁴⁵.

312 To remove the heat accumulated during sliding, velocity damping with a damping coefficient of
313 1.0 ps^{-1} is applied to the relative velocities (with respect to the velocity of the rigid top slider layer)
314 of each atom in the second layer from top (slider) and to the velocities of each atom in the fifth
315 layer from top (substrate). For finite temperature simulations, Langevin thermostats (rather than
316 mere viscous damping) are employed. This mimics the energy dissipation channels (via coupling
317 to implicit external heat baths) through both slider and substrate in experiments, with minor effect
318 on the dynamics of the two layers at the shear plane. In addition, in order to dampen vertical stage
319 oscillations, velocity damping with same damping coefficient of 1.0 ps^{-1} is also applied to the
320 vertical velocities of the atoms in the top slider layer⁴⁶. See Supplementary Note 1 for further details
321 regarding the simulation model and protocols.

324 References

- 325 1 Hod, O., Meyer, E., Zheng, Q. & Urbakh, M. Structural superlubricity and ultralow friction
326 across the length scales. *Nature* **563**, 485-492, (2018).
- 327 2 Berman, D., Erdemir, A. & Sumant, A. V. Approaches for Achieving Superlubricity in Two-
328 Dimensional Materials. *ACS Nano* **12**, 2122-2137, (2018).
- 329 3 Dienwiebel, M. *et al.* Superlubricity of graphite. *Phys. Rev. Lett.* **92**, 126101, (2004).
- 330 4 Liu, Z. *et al.* Observation of microscale superlubricity in graphite. *Phys. Rev. Lett.* **108**, 205503,
331 (2012).
- 332 5 Martin, J. M., Donnet, C., Le Mogne, T. & Epicier, T. Superlubricity of molybdenum
333 disulphide. *Phys. Rev. B* **48**, 10583-10586, (1993).
- 334 6 Martin, J. M. *et al.* Superlubricity of MoS₂: crystal orientation mechanisms. *Surf. Coat.*
335 *Technol.* **68-69**, 427-432, (1994).
- 336 7 Li, H. *et al.* Superlubricity between MoS₂ Monolayers. *Adv. Mater.* **29**, 1701474, (2017).
- 337 8 Leven, I., Krepel, D., Shemesh, O. & Hod, O. Robust Superlubricity in Graphene/h-BN
338 Heterojunctions. *J. Phys. Chem. Lett.* **4**, 115-120, (2013).
- 339 9 Mandelli, D., Leven, I., Hod, O. & Urbakh, M. Sliding friction of graphene/hexagonal-boron
340 nitride heterojunctions: a route to robust superlubricity. *Sci. Rep.* **7**, 10851, (2017).
- 341 10 Song, Y. *et al.* Robust microscale superlubricity in graphite/hexagonal boron nitride layered
342 heterojunctions. *Nat. Mater.* **17**, 894, (2018).
- 343 11 Liu, Y. *et al.* Interlayer Friction and Superlubricity in Single-Crystalline Contact Enabled by
344 Two-Dimensional Flake-Wrapped Atomic Force Microscope Tips. *ACS Nano* **12**, 7638-7646,
345 (2018).

- 346 12 Wang, L. *et al.* Superlubricity of a graphene/MoS₂ heterostructure: a combined experimental
347 and DFT study. *Nanoscale* **9**, 10846-10853, (2017).
- 348 13 Mandelli, D., Ouyang, W., Hod, O. & Urbakh, M. Negative Friction Coefficients in Superlubric
349 Graphite--Hexagonal Boron Nitride Heterojunctions. *Phys. Rev. Lett.* **122**, 076102, (2019).
- 350 14 Yazyev, O. V. & Chen, Y. P. Polycrystalline graphene and other two-dimensional materials.
351 *Nat. Nanotechnol.* **9**, 755, (2014).
- 352 15 Yazyev, O. V. & Louie, S. G. Topological defects in graphene: Dislocations and grain
353 boundaries. *Phys. Rev. B* **81**, 195420, (2010).
- 354 16 Červenka, J. & Flipse, C. F. J. Structural and electronic properties of grain boundaries in
355 graphite: Planes of periodically distributed point defects. *Phys. Rev. B* **79**, 195429, (2009).
- 356 17 Tison, Y. *et al.* Grain Boundaries in Graphene on SiC(000 $\bar{1}$) Substrate. *Nano Lett.* **14**, 6382-
357 6386, (2014).
- 358 18 Gao, X., Ouyang, W., Hod, O. & Urbakh, M. Mechanisms of frictional energy dissipation at
359 graphene grain boundaries. *Phys. Rev. B* **103**, 045418, (2021).
- 360 19 Kavalur, A. & Kim, W. K. Molecular dynamics study on friction of polycrystalline graphene.
361 *Comput. Mater. Sci.* **137**, 346-361, (2017).
- 362 20 Li, H. & Kim, W. K. Role of multigrain structure on friction of graphene layers. *Comput. Mater.*
363 *Sci.* **165**, 23-33, (2019).
- 364 21 Zhang, J. *et al.* Effects of grain boundary on wear of graphene at the nanoscale: A molecular
365 dynamics study. *Carbon* **143**, 578-586, (2019).
- 366 22 Barel, I., Urbakh, M., Jansen, L. & Schirmeisen, A. Multibond Dynamics of Nanoscale Friction:
367 The Role of Temperature. *Phys. Rev. Lett.* **104**, 066104, (2010).
- 368 23 Braun, O. M., Barel, I. & Urbakh, M. Dynamics of Transition from Static to Kinetic Friction.
369 *Phys. Rev. Lett.* **103**, 194301, (2009).
- 370 24 Bouchbinder, E., Brener, E. A., Barel, I. & Urbakh, M. Slow Cracklike Dynamics at the Onset
371 of Frictional Sliding. *Phys. Rev. Lett.* **107**, 235501, (2011).
- 372 25 Rubinstein, S. M., Cohen, G. & Fineberg, J. Detachment fronts and the onset of dynamic
373 friction. *Nature* **430**, 1005-1009, (2004).
- 374 26 Ouyang, W. *et al.* Load and Velocity Dependence of Friction Mediated by Dynamics of
375 Interfacial Contacts. *Phys Rev Lett* **123**, 116102, (2019).
- 376 27 Ouyang, W., Cheng, Y., Ma, M. & Urbakh, M. Load-velocity-temperature relationship in
377 frictional response of microscopic contacts. *J. Mech. Phys. Solids* **137**, 103880, (2020).
- 378 28. Liu, B. *et al.*, Negative friction coefficient in microscale graphite/mica layered heterojunctions.
379 *Sci. Adv.* **6**, eaaz6787 (2020).
- 380 29. We note that the Hemholtz free energy calculations are performed for fixed supercell
381 dimensions, constant number of atoms, and constant temperature. While periodic boundary
382 conditions are applied in all directions, a large vacuum size of 60 Å in the vertical direction was
383 employed, effectively enforcing only lateral periodic boundary conditions. Therefore, the actual
384 vertical dimensions of the 6-layered slab are not fixed during the calculations. Nevertheless, the
385 good agreement between the energy barriers obtained using the dynamical calculations and
386 those obtained using the NEB method (see Supplementary Note 5) indicates that the dynamical
387 results represent the Helmholtz free energy sufficiently well, despite the minor volume
388 flexibility under normal load.
- 389 30. Prandtl, L. Ein Gedankenmodell zur kinetischen Theorie der festen Körper. *Z. Angew. Math.*
390 *Mech.* **8**, 85-106 (1928).
- 391 31. Tomlinson, G. A. CVI. A molecular theory of friction. *Philos. Mag.* **7**, 905-939 (1929).
- 392 32. Vanossi, A., Manini, N., Urbakh, M., Zapperi, S. & Tosatti, E. Colloquium: Modeling friction:
393 From nanoscale to mesoscale. *Rev. Mod. Phys.* **85**, 529-552, (2013).
- 394 33. Qu, C. *et al.* Origin of Friction in Superlubric Graphite Contacts. *Phys. Rev. Lett.* **125**, 126102,
395 (2020).

- 396 34. Koren, E., Lörtscher, E., Rawlings, C., Knoll, A. W. & Duerig, U. Adhesion and friction in
397 mesoscopic graphite contacts. *Science* **348**, 679, (2015).
- 398 35. Chen, Z., Khajeh, A., Martini, A. & Kim, S. H. Chemical and physical origins of friction on
399 surfaces with atomic steps. *Sci. Adv.* **5**, eaaw0513 (2019).
- 400 36. Ophus, C., Shekhawat, A., Rasool, H. & Zettl, A. Large-scale experimental and theoretical
401 study of graphene grain boundary structures. *Phys. Rev. B* **92**, 205402, (2015).
- 402 37. Shekhawat, A. & Ritchie, R. O. Toughness and strength of nanocrystalline graphene. *Nat.*
403 *Commun.* **7**, 10546, (2016).
- 404 38. Brenner, D. W. *et al.* A second-generation reactive empirical bond order (REBO) potential
405 energy expression for hydrocarbons. *J. Phys.: Condens. Matter* **14**, 783-802, (2002).
- 406 39. Kolmogorov, A. N. & Crespi, V. H. Registry-dependent interlayer potential for graphitic
407 systems. *Phys. Rev. B* **71**, 235415, (2005).
- 408 40. Leven, I., Azuri, I., Kronik, L. & Hod, O. Inter-layer potential for hexagonal boron nitride. *J.*
409 *Chem. Phys.* **140**, 104106, (2014).
- 410 41. Leven, I., Maaravi, T., Azuri, I., Kronik, L. & Hod, O. Interlayer Potential for Graphene/h-BN
411 Heterostructures. *J. Chem. Theory Comput.* **12**, 2896-2905, (2016).
- 412 42. Maaravi, T., Leven, I., Azuri, I., Kronik, L. & Hod, O. Interlayer Potential for Homogeneous
413 Graphene and Hexagonal Boron Nitride Systems: Reparametrization for Many-Body
414 Dispersion Effects. *J. Phys. Chem. C* **121**, 22826-22835, (2017).
- 415 43. Ouyang, W., Mandelli, D., Urbakh, M. & Hod, O. Nanoserpents: Graphene Nanoribbon Motion
416 on Two-Dimensional Hexagonal Materials. *Nano Lett.* **18**, 6009-6016, (2018).
- 417 44. Ouyang, W. *et al.* Mechanical and Tribological Properties of Layered Materials under High
418 Pressure: Assessing the Importance of Many-Body Dispersion Effects. *J Chem Theory Comput*
419 **16**, 666-676, (2020).
- 420 45. Plimpton, S. Fast Parallel Algorithms for Short-Range Molecular Dynamics. *J. Comput. Phys.*
421 **117**, 1-19, (1995).
- 422 46. Ouyang, W., Ma, M., Zheng, Q. & Urbakh, M. Frictional Properties of Nanojunctions Including
423 Atomically Thin Sheets. *Nano Lett.* **16**, 1878-1883, (2016).

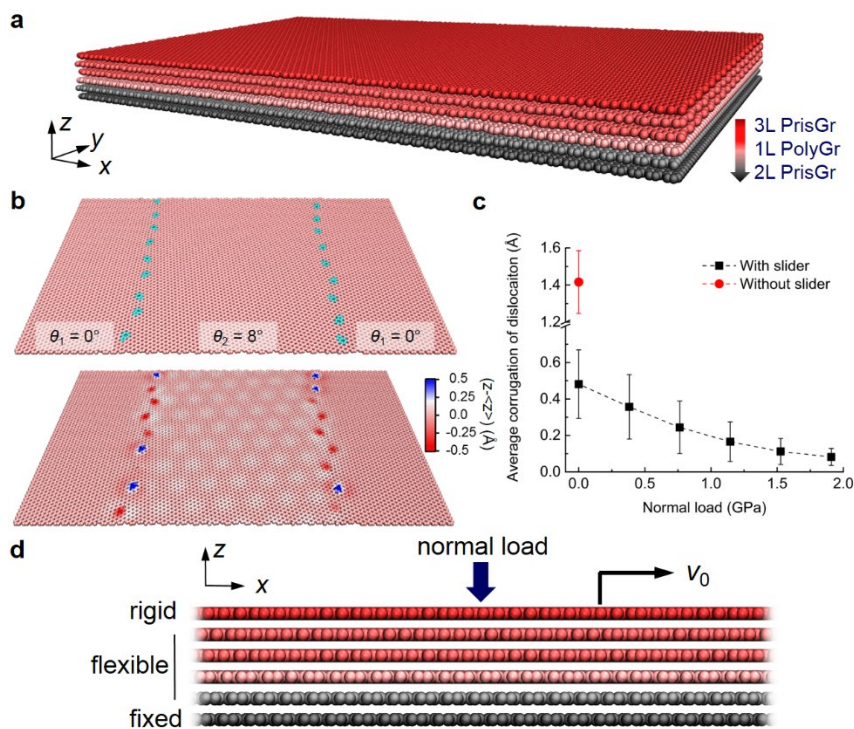
424 **Acknowledgments**

425 X.G. acknowledges the fellowship from the Sackler Center for Computational Molecular and
426 Materials Science at Tel Aviv University. W.O. acknowledges the financial support from the
427 National Natural Science Foundation of China (No. 11890673 and No. 11890674). O.H. is grateful
428 for the generous financial support of the Israel Science Foundation under Grant No. 1586/17 and
429 the Naomi Foundation for generous financial support via the 2017 Kadar Award. M.U.
430 acknowledges the financial support of the Israel Science Foundation, Grant No. 1141/18 and the
431 binational program of the National Science Foundation of China and Israel Science Foundation,
432 Grant No. 3191/19. M.U. and O.H. thank partial computational support of the Tel Aviv University
433 Center for Nanoscience and Nanotechnology.

434
435 **Author contributions:** O.H and M.U. designed research, X.G. performed research, X.G., W.O.,
436 M.U., and O.H. analyzed data, X.G., W.O., M.U., and O.H. wrote the paper.

437
438 **Competing interests:** The authors declare that they have no competing interests.

439
440 **Data availability:** The data that support the findings of the present study are available within the
441 paper and its Supplementary file. Other data are available from the corresponding authors upon
442 request.



445

446

447

448

449

450

451

452

453

454

455

456

457

458

459

460

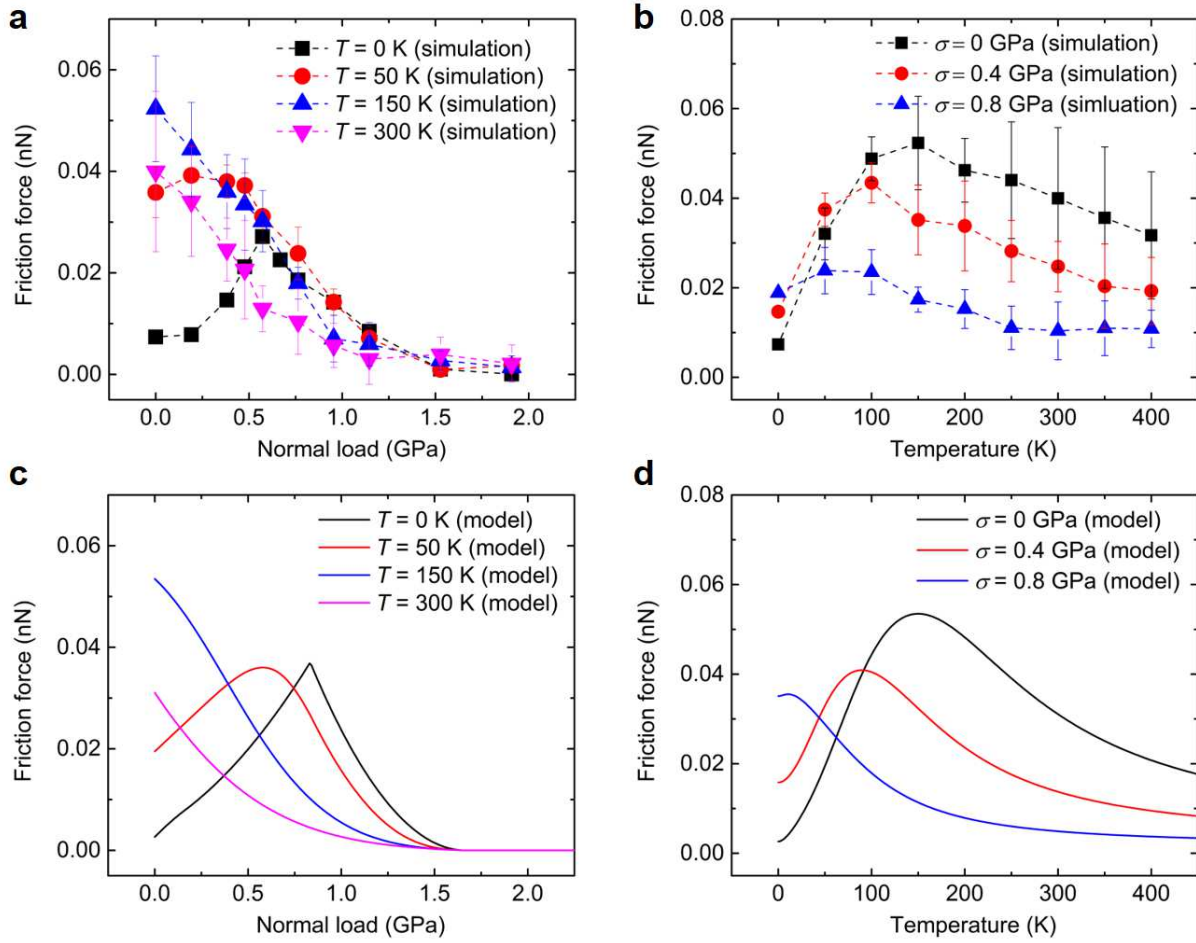
461

462

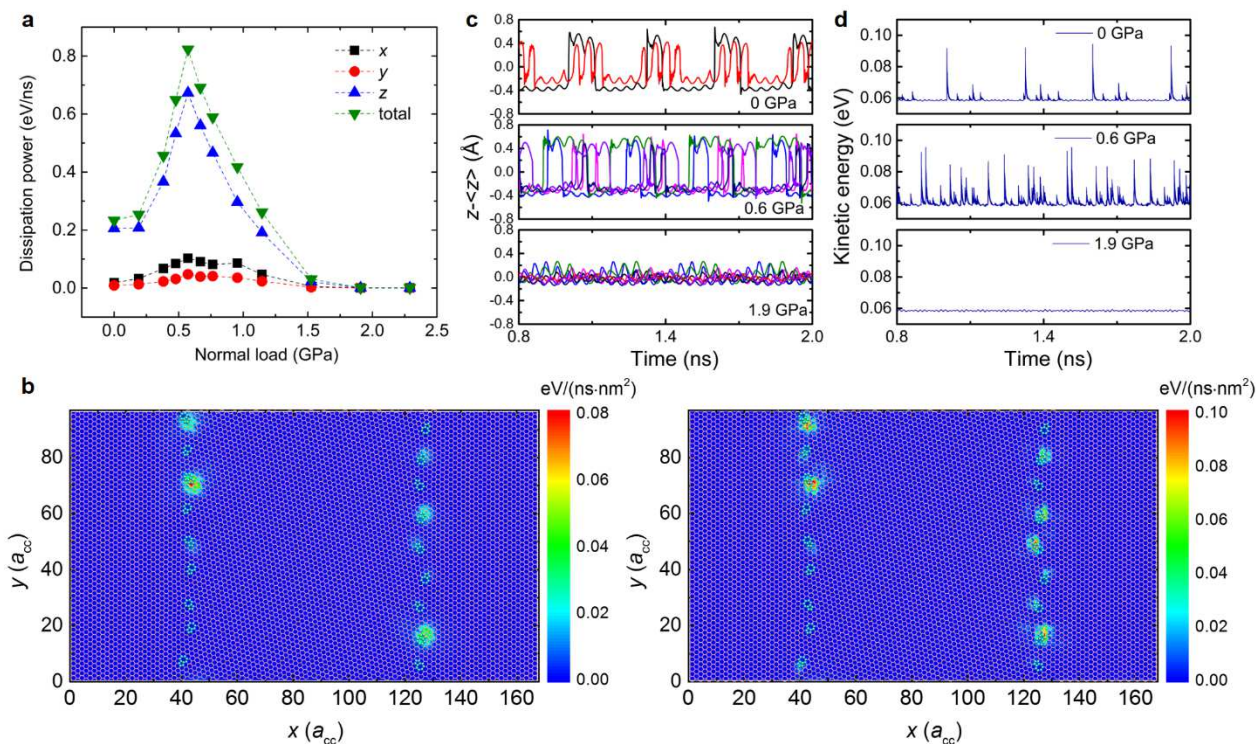
463

464

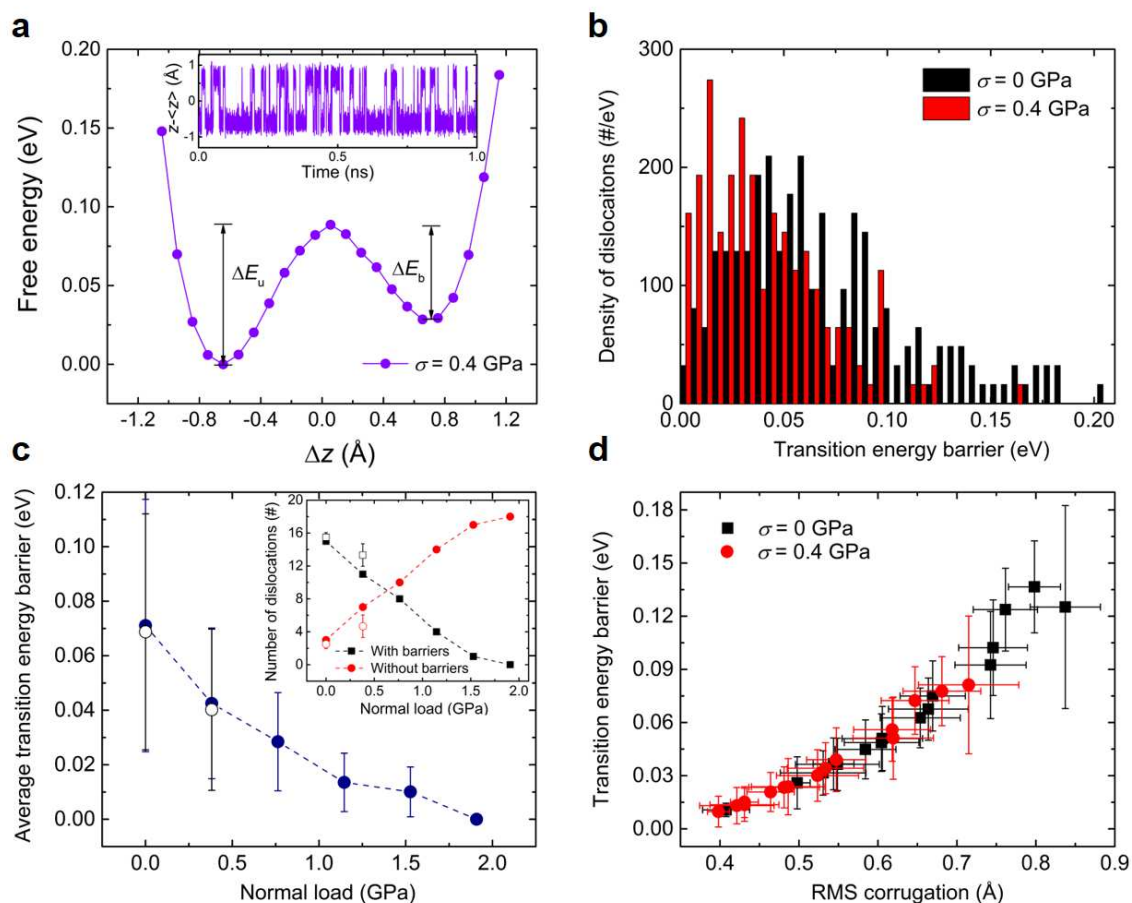
Fig. 1. Molecular dynamics simulation model and setup. **a** A perspective view of the model system. From top to bottom, the system contains three layers of Bernal stacked pristine graphene (red spheres) with orientation angle $\theta_0 = 38.2^\circ$, one layer of polycrystalline graphene (pink and cyan spheres) with orientation angles $\theta_1 = 0^\circ$ and $\theta_2 = 8^\circ$ for the two patches in the layer, and two layers of pristine graphene (grey spheres) with orientation angle $\theta_3 = 0^\circ$. The dark red and grey colored spheres indicate the rigid top layer and the fixed bottom layer atoms, respectively. Periodic boundary conditions are applied along both lateral directions. **b** The atomic structure and annealed topography of the polycrystalline graphene layer within the stack. The lower panel shows the surface corrugation at zero normal load with respect to the average height, $\langle z \rangle$, of the two grains. **c** The average dislocation corrugation as a function of normal load (black squares). As reference, we present the corresponding corrugation calculated in the absence of the slider (red circle). The error bars present standard deviations, obtained by averaging over all the dislocations. **d** Friction simulation setup. During the simulations, the top rigid layer is shifted at a constant velocity $v_0 = 5$ m/s along the x axis direction (the armchair direction of the pristine graphene substrate layers). Normal load is applied to the top layer by adding a uniform force to each of the atoms. The bottom layer is kept rigid and fixed in place throughout the motion. The dynamics of all other atoms follows the REBO intralayer potential and the registry-dependent interlayer potential and subjected to damped dynamics at zero temperature or Langevin thermostats at finite temperatures, as detailed in the Methods section and in Supplementary Note 1.



465
 466 **Fig. 2. Load and temperature dependence of friction.** Molecular dynamics simulation results of
 467 **a** load dependence of friction at representative temperatures of $T = 0, 50, 150,$ and 300 K and **b**
 468 temperature dependence of friction at representative normal loads of $\sigma = 0, 0.4,$ and 0.8 GPa for the
 469 model system presented in Fig. 1. Here, the supercell contains a total grain boundary of length
 470 ~ 28 nm. **c** and **d** show results obtained using the phenomenological model for **c** the load
 471 dependence of friction at several temperatures, and **d** the temperature dependence of friction at
 472 under several normal loads. The model parameters extracted from the dynamical simulations, are:
 473 $\Delta E_1 = 0.01$ eV, $\Delta E_2 = 0.1$ eV, $\alpha_1 = 0.06$ eV/GPa, $\alpha_2 = 0.03$ eV/GPa, $\beta = 0.3,$ $c_0 =$
 474 0.005 eV, $\Delta x = 10.8$ Å, $f_0 = 1.5 \times 10^{11}$ s $^{-1}$, $N = 18,$ and $v_0 = 5$ m/s. Representative lateral
 475 force traces at different normal loads and temperatures, and the convergence of friction calculation
 476 can be found in Supplementary Note 2. Additional details regarding the phenomenological model
 477 are given in Supplementary Note 7.



479 **Fig. 3. Mechanism of the load dependence of frictional dissipation at zero temperature.** **a** Total
 480 dissipation power and its directional contributions (x , y , z – see Fig. 1a.) as a function of normal
 481 load. **b** Spatial distributions of dissipation power density in the z direction of the second pristine
 482 layer (left panel) and the fifth pristine layer (right panel) under the normal load of 0.6 GPa. The
 483 geometric configuration of the PolyGr layer is superimposed on the 2D maps. The pentagon-
 484 heptagon atoms are shown in cyan and the hexagon carbon atoms are represented in pink. The
 485 power density is calculated based on area elements with size of a_{cc}^2 ($a_{cc} = 1.42039 \text{ \AA}$ is the
 486 equilibrium C-C bond length in REBO potential). **c** Representative dislocation trajectories (for two
 487 sliding periods at steady-state) corresponding to the out-of-plane motion of the atoms with maximal
 488 RMS corrugation within each dislocation (different colors correspond to different dislocations)
 489 during sliding, under normal loads of 0, 0.6, and 1.9 GPa (from top to bottom panels, respectively).
 490 Substantial buckling and unbuckling dynamics during sliding is observed under normal loads of 0
 491 and 0.6 GPa. **d** Kinetic energy profiles corresponding to the traces appearing in panel c. More
 492 details regarding the temperature effects on dislocation buckling can be found in Supplementary
 493 Note 4. Movies of typical simulations are also provided in the Supplementary Information.



496
 497 **Fig. 4. Dislocation buckling transition energy barriers.** **a** An example of a free energy profile of
 498 one dislocation calculated under a normal load of 0.4 GPa at the initial configuration (prior to
 499 sliding). The inset shows a 1 ns atomic out-of-plane motion trajectory of the dislocation during the
 500 equilibrium simulation. **b** The number density distribution of non-zero transition energy barrier
 501 dislocations (spatially averaged over six equidistant slider positions along one sliding period)
 502 calculated under normal loads of 0 (black bars) and 0.4 GPa (red bars). **c** The average transition
 503 energy barrier as a function of normal load. The average values (full symbols) and error bars
 504 (standard deviation of the distribution presented in panel b) are calculated at the initial configuration
 505 over all dislocations of transition energy barriers above 0.0026 eV. The empty data points represent
 506 the spatial average results (over six interlayer positions within the sliding period), producing
 507 essentially the same results within the given error bars. The inset shows the number of dislocations
 508 with barriers smaller (full red circles) or higher (full black squares) than 0.0026 eV, as a function
 509 of normal load. The empty symbols present the spatially averaged results. **d** Correlation between
 510 dislocation corrugation and its transition energy barrier calculated under normal loads of 0 (black
 511 squares) and 0.4 GPa (red circles). The calculation is performed separately for each dislocation,
 512 spatially averaged over six equidistant slider positions along one sliding period as in panel b. All
 513 calculations presented in this figure were performed at $T = 300$ K.

Figures

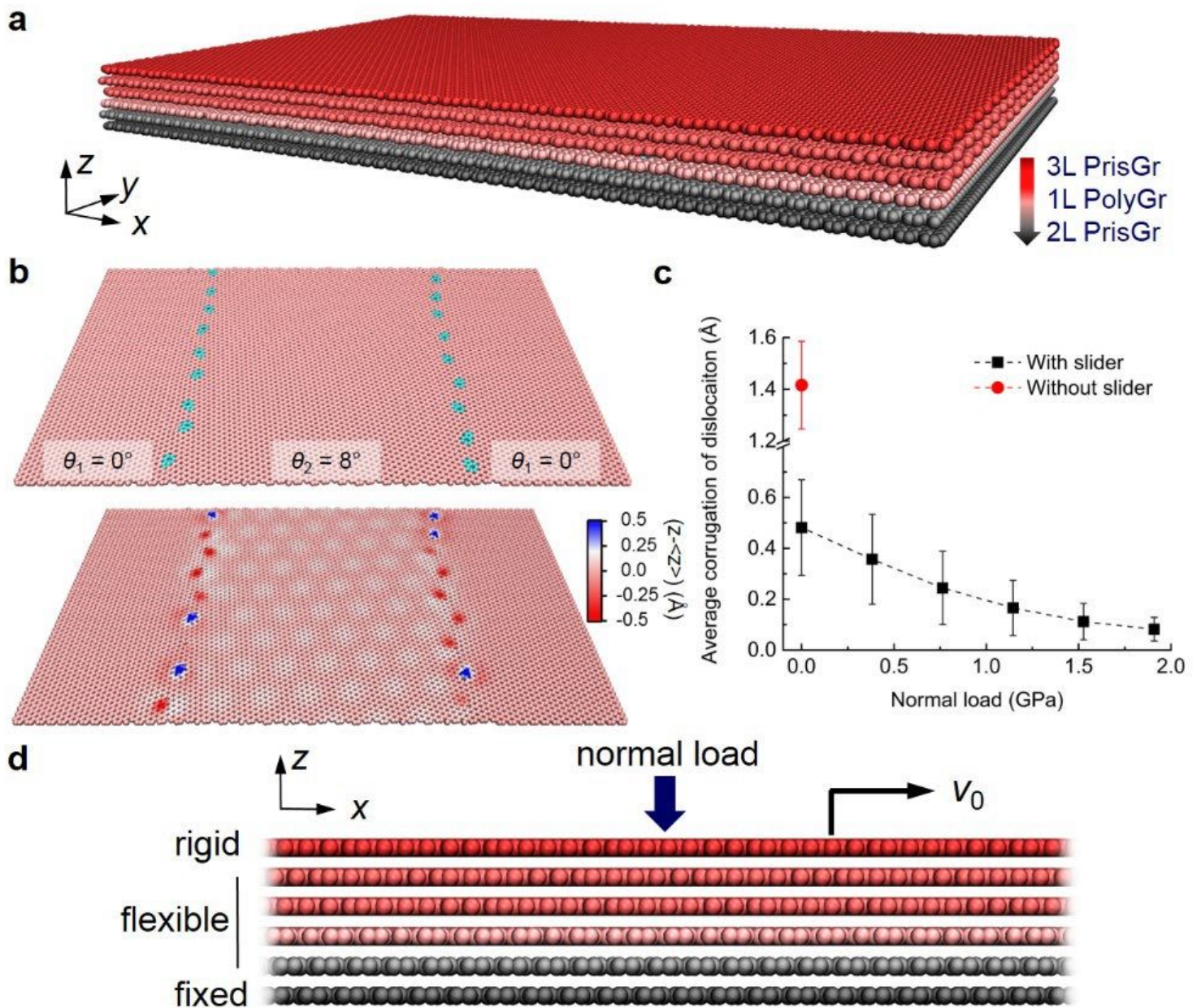


Figure 1

Molecular dynamics simulation model and setup. a A perspective view of the model system. From top to bottom, the system contains three layers of Bernal stacked pristine graphene (red spheres) with orientation angle $\theta_0 = 38.2^\circ$, one layer of polycrystalline graphene (pink and cyan spheres) with orientation angles $\theta_1 = 0^\circ$ and $\theta_2 = 8^\circ$ for the two patches in the layer, and two layers of pristine graphene (grey spheres) with orientation angle $\theta_3 = 0^\circ$. The dark red and grey colored spheres indicate the rigid top layer and the fixed bottom layer atoms, respectively. Periodic boundary conditions are applied along both lateral directions. b The atomic structure and annealed topography of the polycrystalline graphene layer within the stack. The lower panel shows the surface corrugation at zero normal load with respect to the

average height, $\langle h \rangle$, of the two grains. c The average dislocation corrugation as a function of normal load (black squares). As reference, we present the corresponding corrugation calculated in the absence of the slider (red circle). The error bars present standard deviations, obtained by averaging over all the dislocations. d Friction simulation setup. During the simulations, the top rigid layer is shifted at a constant velocity $v_0=5$ ms $^{-1}$ along the x axis direction (the armchair direction of the pristine graphene substrate layers). Normal load is applied to the top layer by adding a uniform force to each of the atoms. The bottom layer is kept rigid and fixed in place throughout the motion. The dynamics of all other atoms follows the REBO intralayer potential and the registry-dependent interlayer potential and subjected to damped dynamics at zero temperature or Langevin thermostats at finite temperatures, as detailed in the Methods section and in Supplementary Note 1.

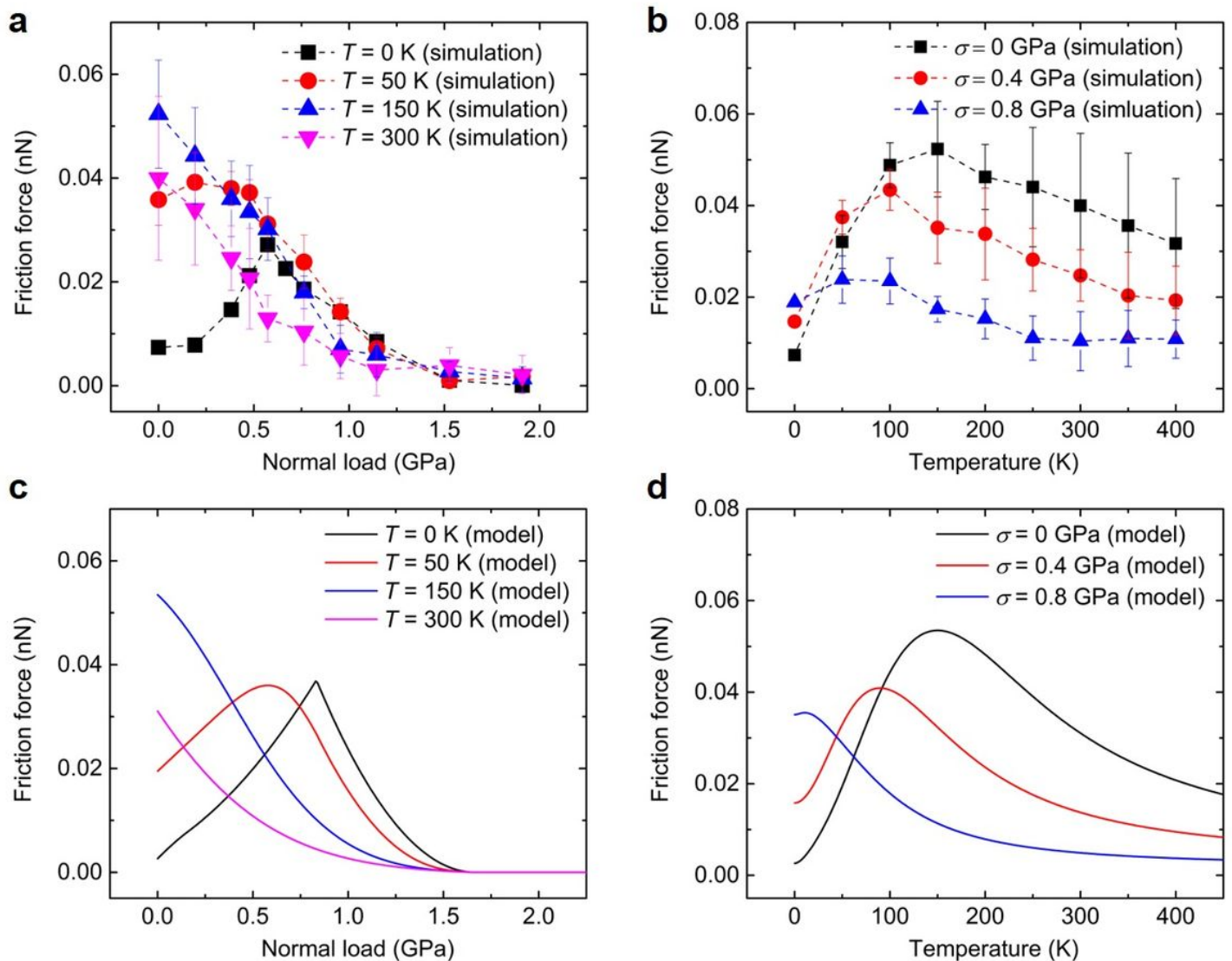


Figure 2

Load and temperature dependence of friction. Molecular dynamics simulation results of a load dependence of friction at representative temperatures of $T = 0, 50, 150,$ and 300 K and b temperature dependence of friction at representative normal loads of $\sigma = 0, 0.4,$ and 0.8 GPa for the model system

presented in Fig. 1. Here, the supercell contains a total grain boundary of length ~ 28 nm. c and d show results obtained using the phenomenological model for c the load dependence of friction at several temperatures, and d the temperature dependence of friction at under several normal loads. The model parameters extracted from the dynamical simulations, are: $\Delta\epsilon_1=0.01$ eV, $\Delta\epsilon_2=0.1$ eV, $\epsilon_1=0.06$ eV/GPa, $\epsilon_2=0.03$ eV/GPa, $\epsilon=0.3$, $\epsilon_0=0.005$ eV, $\Delta\epsilon=10.8$ Å, $\epsilon_0=1.5 \times 10^{11}$ s $^{-1}$, $\epsilon=18$, and $\epsilon_0=5$ ms.

Representative lateral force traces at different normal loads and temperatures, and the convergence of friction calculation can be found in Supplementary Note 2. Additional details regarding the phenomenological model are given in Supplementary Note 7.

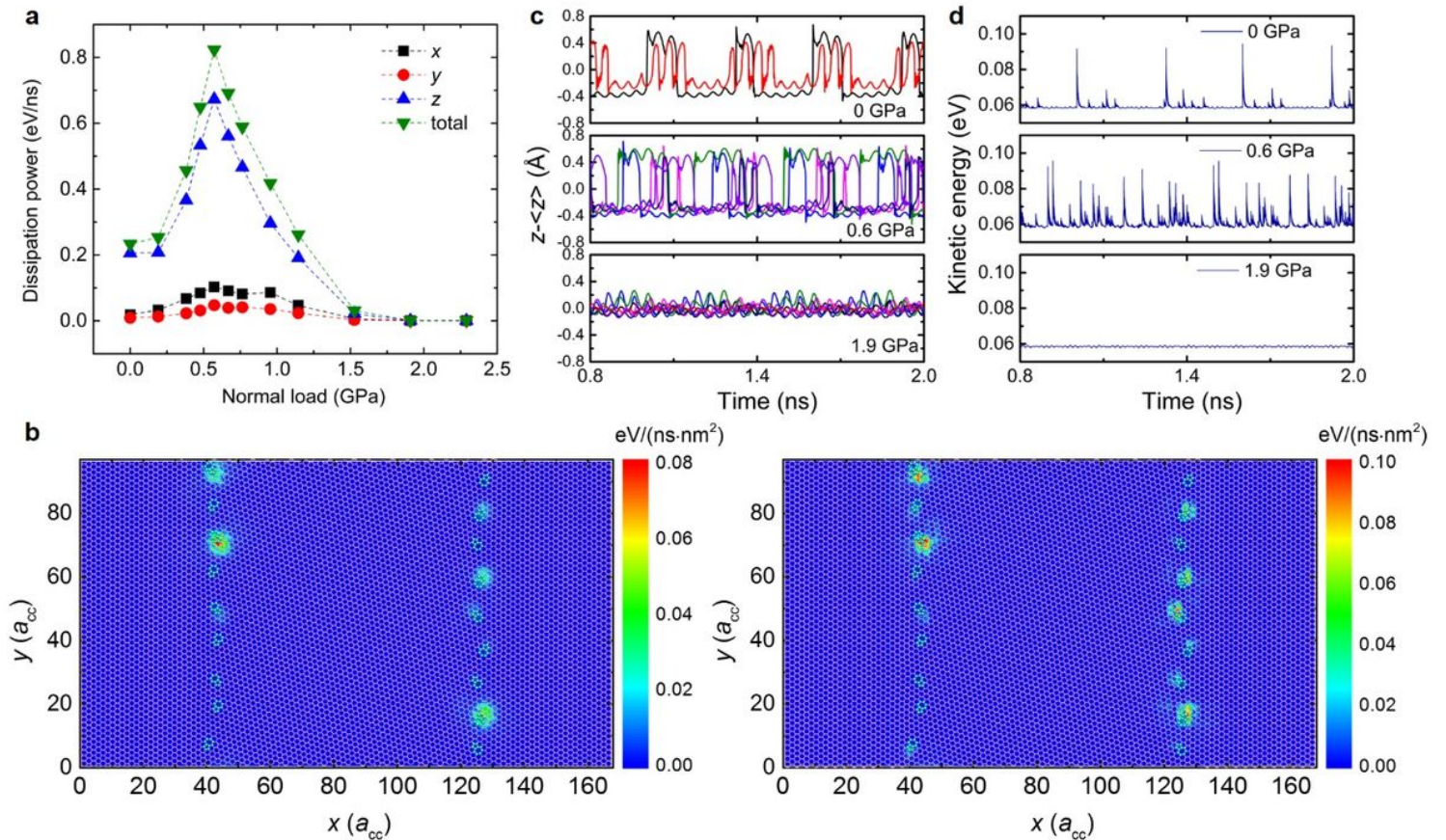


Figure 3

Mechanism of the load dependence of frictional dissipation at zero temperature. a Total 4dissipation power and its directional contributions (x, y, z – see Fig. 1a.) as a function of normal load. b Spatial distributions of dissipation power density in the z direction of the second pristine layer (left panel) and the fifth pristine layer (right panel) under the normal load of 0.6 GPa. The geometric configuration of the PolyGr layer is superimposed on the 2D maps. The pentagon-heptagon atoms are shown in cyan and the hexagon carbon atoms are represented in pink. The power density is calculated based on area elements with size of ϵ_{cc}^2 ($\epsilon_{cc}=1.42039$ Å is the equilibrium C-C bond length in REBO potential). c Representative dislocation trajectories (for two sliding periods at steady-state) corresponding to the out-of-plane motion of the atoms with maximal RMS corrugation within each dislocation (different colors correspond to different dislocations) during sliding, under normal loads of 0,0.6, and 1.9 GPa (from top to bottom panels, respectively). Substantial buckling and unbuckling dynamics during sliding is observed under

normal loads of 0 and 0.6 GPa. d Kinetic energy profiles corresponding to the traces appearing in panel c. More details regarding the temperature effects on dislocation buckling can be found in Supplementary Note 4. Movies of typical simulations are also provided in the Supplementary Information.

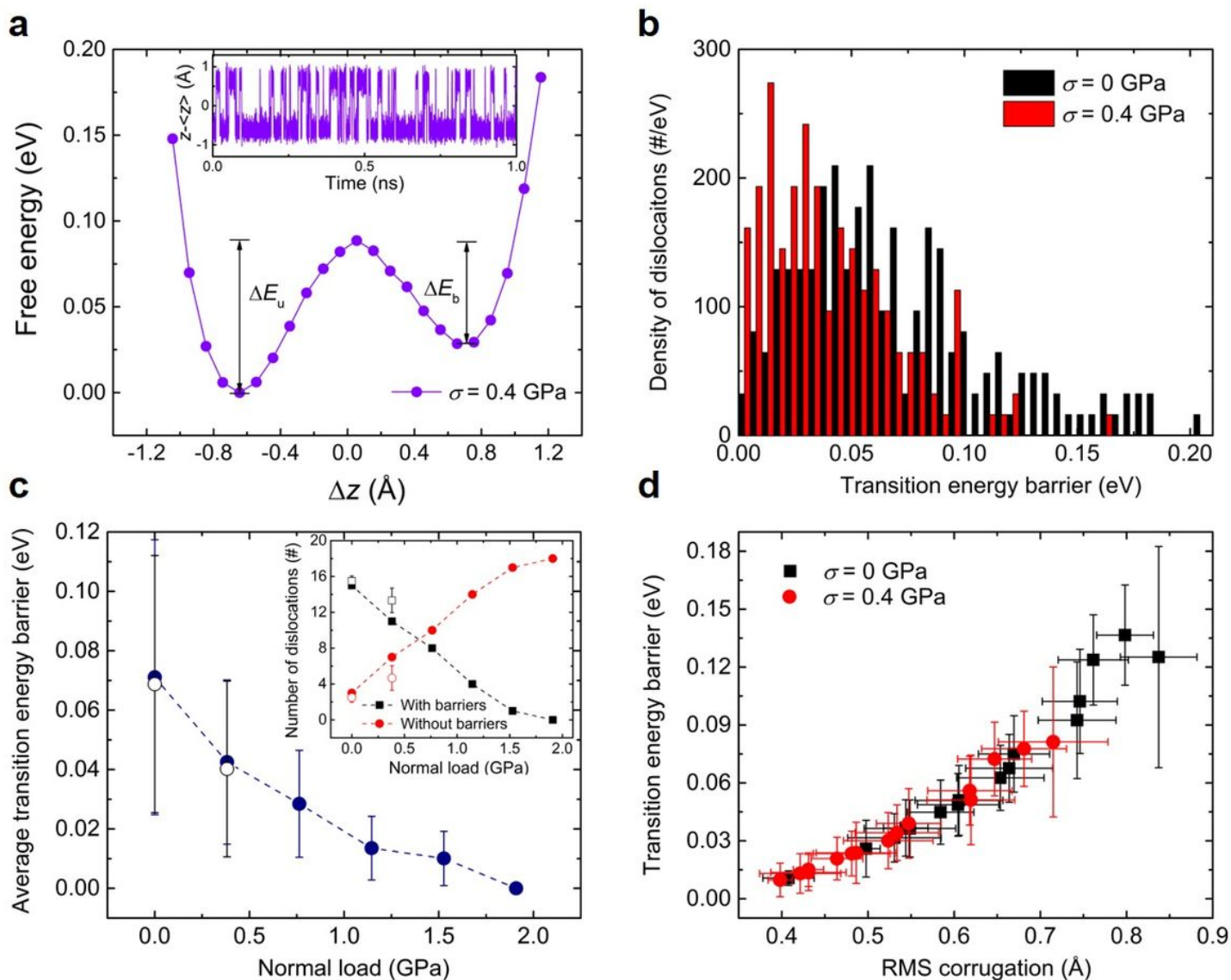


Figure 4

Dislocation buckling transition energy barriers. a An example of a free energy profile of one dislocation calculated under a normal load of 0.4 GPa at the initial configuration (prior to sliding). The inset shows a 1 ns atomic out-of-plane motion trajectory of the dislocation during the equilibrium simulation. b The number density distribution of non-zero transition energy barrier dislocations (spatially averaged over six equidistant slider positions along one sliding period) calculated under normal loads of 0 (black bars) and 0.4 GPa (red bars). c The average transition energy barrier as a function of normal load. The average values (full symbols) and error bars (standard deviation of the distribution presented in panel b) are calculated at the initial configuration over all dislocations of transition energy barriers above 0.0026 eV. The empty data points represent the spatial average results (over six interlayer positions within the sliding period), producing essentially the same results within the given error bars. The inset shows the number of

dislocations with barriers smaller (full red circles) or higher (full black squares) than 0.0026 eV, as a function of normal load. The empty symbols present the spatially averaged results. d Correlation between dislocation corrugation and its transition energy barrier calculated under normal loads of 0 (black squares) and 0.4 GPa (red circles). The calculation is performed separately for each dislocation, spatially averaged over six equidistant slider positions along one sliding period as in panel b. All calculations presented in this figure were performed at $T=300$ K.

Supplementary Files

This is a list of supplementary files associated with this preprint. Click to download.

- [MovieSM1.mp4](#)
- [MovieSM2.mp4](#)
- [MovieSM3.mp4](#)
- [MovieSM4.mp4](#)
- [MovieSM5.mp4](#)
- [MovieSM6.mp4](#)
- [graphene.grain.boudaries.PBC.SM.nature.commun..2021.03.18.pdf](#)